TECHNICAL MEMORANDUM

330

Rain detection over land surfaces using passive microwave satellite data

P. Bauer

Research Department

January 2001

European Centre for Medium-Range Weather Forecasts
Europäisches Zentrum für mittelfristige Wettervorhersage
Centre européen pour les prévisions météorologiques à moyen

Abstract

An algorithm is presented for the detection of surface rainfall using passive microwave measurements by satellite radiometers. The technique consists of a two-stage approach to distinguish precipitation signatures from other effects: (1) Contributions from slowly varying parameters (surface type and state) are isolated by comparing observed brightness temperatures to those obtained from previous orbits only containing rain-free observations. (2) Effects of more dynamic parameters, i.e., surface temperature and moisture, are reduced by successive subtraction from the observations by means of principal component analysis. For this purpose, the general signatures of both temperature and moisture variations are deduced from radiative transfer simulations. The fundamentals of this approach are based on a methodology developed by Conner and Petty (1998). The technique is applied to TMI observations and compared to co-located measurements of TMI and PR as well as independent techniques over selected regions in Africa, North and South America, as well as India. All techniques provide similar rainfall screening skill where our technique showed superior results over Africa, North America, and India. Based on Heidke skill scores as a function of rainfall and brightness temperature range, an efficient calibration tool to retrieve near-surface rainfall intensities is provided.

1 Introduction

Rainfall estimation from satellite data over land surfaces still represents a challenge because neither at visible/infrared (VIS/IR) nor at microwave wavelengths (MW) do raindrops provide significant contributions to the total signal to allow a direct estimation of rainrate. Principally, cloud top temperature and reflectivity is related to time-space averages of surface rainfall in VIS/IR methods. The loose physical connection between these quantities prohibits an instantaneous estimate. At microwaves, surface emissivity is high and spatially variable which increases the uncertainty of the atmospheric contribution estimate. Here, mainly scattering by precipitating ice provides the main information on surface rainfall. However, since the beginning of VIS/IR and MW remote sensing both data sources are exploited (Petty 1995). Recent accuracy assessments indicate average errors of at best 50-100% with a strong dependence on season and region as well as dataset resolution (Barrett et al. 1995, Smith et al. 1998). Thus algorithm improvements are only achieved if local surface conditions are accounted for and if the signal to rainrate relationship is based on data which is more representative of global rainfall system variability.

With the launch of the Tropical Rainfall Measuring Mission in November 1997, the first spaceborne precipitation radar (PR) became available (Kummerow et al. 1998). It is a single-frequency (13.8 GHz), electronically scanning radar with nominal resolutions of 4.3 km and 0.25 km in the horizontal and vertical dimensions, respectively. The cross-track scan pattern covers a 215 km swath consisting of 49 beams along a scan angle of $\pm$ 17 ^{o}. Its sensitivity is specified with 0.7 $mm\ h^{-1}$ with a calibration accuracy of $\sim$ 0.8 dB. A microwave radiometer is available on the same platform (TRMM Microwave Imager, TMI) providing measurements at 10.65, 19.35, 21.3, 37.0, and 85.5 GHz on a conical scan with a nearly constant surface incidence angle of 52.8^o and a swath width of 760 km. All channels measure vertically and horizontally polarized radiances (expressed as equivalent black body temperatures, TB) except the 21.3 GHz channel which only measures vertically polarized radiances. Since only one antenna is used for all channels the spatial resolution of the effective field of view (EFOV) depends on frequency and ranges from 37 km x 63 km at 10.65 GHz to 5 km x 7 km at 85.5 GHz. The TRMM orbit is non-sunsynchronous and covers latitudes between 38°N and 38°S. Thus the combination of both sensors provides an excellent tool for the evaluation of available rainfall detection and estimation techniques as well as for new developments.

The difficult microwave signal interpretation over land surfaces has favoured somewhat the implementation of empirical algorithms which make use of co-located satellite and ground-based (radar) observations to derive a calibration of satellite measurements by reference data (e.g. Ferraro and Marks 1995). For large-scale regional or even global applications this approach is hampered by the

limited representativity of available calibration data sets. Thus co-located radiometric and radar measurements from TRMM provide an outstanding data source covering tropical and subtropical latitudes over various climatological regimes.

The technique presented here makes use of a first-order approach to remove seasonally varying surface contributions from instantaneous TMI measurements by generating maps of clear-sky temporal averages of brightness temperatures over various continents, i.e., Africa, India, North and South America. Effects of surface skin temperature and moisture are removed to achieve an increased sensitivity to low rainfall rates according to local conditions. The outline of the technique is presented in Section 2. In Section 3, case studies are presented including retrievals over monthly time scales. The paper is concluded by summary and discussion.

In the following, rainfall intensity is always treated in terms of rain liquid water content (LWC) to avoid uncertainties imposed by the somewhat uncertain drop size distributions and the dependence of rainfall rate calculation on fallspeed parameterization. Additionally, both scattering ($\propto D^6$) and emission ($\propto D^3$) are closer related to liquid water and ice volume densities (where D denotes particle diameter).

2 Methodology

2.1 Background fields

The algorithm implies that both rather slowly varying and more quickly varying changes of TBs occur over time and space. While the latter include effects of surface temperature and moisture as well as precipitation, the more slowly varying changes are caused by vegetation growth and decay or land use changes. Due to the lack of accurate input data as well as models to describe these variations, averaged TB distributions from cloud-free observations were generated employing the globally applicable screening algorithm founded by Grody (1991) and refined by Ferraro and Marks (1995). Based on this, all observations contaminated by wet land, precipitation, and snowcover were removed.

The averaging was carried out for two periods: period 1 from 18/08/98-02/09/98 (241 orbits) and period 2 from 13/12/99-05/01/00 (373 orbits) with a $(0.25^o)^2$ spatial resolution. All further analyses were restricted to four areas which cover different surface and vegetation types as well as precipitation regimes. Effects of orography on surface emissivity (e.g. M"atzler and Standley 1999) were not accounted for because of the comparably low spatial grid resolution. From tests maximum deviations of $\pm 5^o$ from the nominal zenith angle were found producing TB variations below 2 K (Burose 2000).

Figs. 1 and 2 show examples of average TBs and their standard deviations from period 1 over the four regions at 85.5 GHz (horizontal polarization). The features are rather smooth and variations are mainly introduced by open water surfaces (due to varying EFOV locations over time) and snow together with undetected light rainfall and clouds. In the following, only those observations are analyzed for which the standard deviation of the background TBs are < 10 K at 10.65 GHz to restrict the investigation to homogeneous surfaces.

2.2 TMI principal components

TBs at different frequencies are usually positively correlated, in particular over land surfaces where the background signal is rather strong. Only in case of scattering by precipitating ice the higher frequency measurements are negatively correlated to those at lower frequencies. The full set of available channels carries therefore some redundant information. The dimension of the input data set (9 for the TMI) may be reduced by means of principal components.

The collection of TB-vectors from observations or simulations was therefore decomposed into independent vectors by calculation of the covariance matrix of differences between the TBs and their background values, i.e., $\delta\mathbf{TB_o} = \mathbf{TB_o} - \overline{\mathbf{TB_o}}$. Then, a matrix of eigenvectors, $\mathbf{E_o}$, can be computed. The EOFs are like the TBs a matrix composed of m measurements / simulations and n channels:

$$\mathbf{EOF_o} = \mathbf{TB_o}\,\mathbf{E_o} \tag{1}$$

EOFs are orthogonal to each other in vector space, i.e.:

$$\sum_n EOF_i EOF_j = 0 \tag{2}$$

while:

$$\sum_n TB_i TB_j \neq 0 \tag{3}$$

for $i, j = 1, n$ and $i \neq j$. Moreover, the associated eigenvalues, λ_i, provide the contribution of each EOF to the total variability in decreasing order. The first EOF represents the largest contribution to total variability, the second EOF the second largest etc. In case of TMI TBs, the λ of the first three EOFs usually sum up to more than 98% of the total variability.

2.3 Temperature and moisture effects

The idea of surface effect correction by generating datasets where either temperature or moisture dominate the signal and which are subtracted from the actual observation signal by orthogonalization follows the approach of Conner and Petty (1998). For each observation, the departure from the background signature is corrected by:

$$\begin{aligned}\delta\mathbf{TB_o}' = \delta\mathbf{TB_o} \quad &- \quad <\delta\mathbf{TB_o}, \mathbf{e_t}>\mathbf{e_t} \\ &- \quad <\delta\mathbf{TB_o}, \mathbf{e_m}>\mathbf{e_m}\end{aligned} \tag{4}$$

$\mathbf{e_{t,m}}$ denote the first eigenvectors of the synthetic temperature (t) or moisture (m) correction data set originating from simulations as explained below while $<.,.>$ denotes an inner product. Thus the second and third terms on the right-hand side of the equation represent the signatures from the unwanted contribution projected into TB-space.

The final objective is therefore the reduction of the orginial TB departure to its equivalent only containing precipitation information. Thus (4) has to be carried out to cancel out both temperature and moisture effects. Only the first EOF is used since it is assumed that the isolation of individual signatures (of temperature etc.) is successful so that the first EOF contains all information of this variables thus a very high explained variance.

In contrast to Conner and Petty's method, we only use radiative transfer simulations in the correction because observations–in particular over land surfaces–always suffer from insufficient screening of unwanted effects either from the surface or from the atmosphere. Since the synthetic datasets used for setting up the eigenvectors for correction in (4) are supposed to show *only* the signature of either surface temperature or moisture, remaining other effects represent a serious problem. For example, if data containing precipitation is included, the correction suppresses precipitation signatures in the observations even though aiming at precipitation estimation. Thus simulations provide a significant advantage over observations. Finally, the moisture dataset is not corrected for temperature contributions as was necessary in Conner and Petty's approach.

Radiative transfer simulations were carried out for cloud-free atmospheres using radiosonde observations of temperature and humidity profiles combined with a semi-empirical surface emissivity

model (e.g. Bauer and Grody 1995). The model was employed in a simplified version which allows to estimate vertically and horizontally polarized surface emissivities at the desired frequencies as a function of skin temperature, fractional coverage of vegetation and water as well as surface roughness. The absolute model accuracy is questionable; however, in this study we only aim at relative effects of temperature and moisture on TBs. Two datasets were generated:

- Temperature: Differences between TBs from similar profiles and for identical surface conditions were calculated where only the skin temperature was modified to +5 K and -5K of the temperature of the lowest atmospheric layer. Through the profiles, vegetation coverage was randomly varied between 0 and 1, water coverage was set to 0, and roughness was varied between 0 and 0.1 cm, respectively.
- Moisture: As above but for identical skin temperatures using fractional water coverages of 0.5 and 0 (dry land).

After calculation of covariance matrices and eigenvectors, the explained variance by the first EOF was 89% for the temperature and 86% for the moisture dataset. Finally, corrections were applied with (4) to all observations from both periods and all regions. From this, eigenvectors, i.e. $\mathbf{e_p}$, p=precipitation) were calculated assuming only precipitation signatures are left.

Results for the first three EOFs and all regions are displayed in Figs. 3 and 4 for periods 1 and 2. One common feature is the decrease of $\mathbf{e_p}$ with frequency in the first EOF. This is fairly independent of region as well as time period suggesting a globally constant $\mathbf{e_p}$. The explained variance, however, has a rather strong dependence on region and period, ranging from 61% to 87%. A possible explanation is the variability in the atmosphere due to cloud water and water vapor indicated by positive $\mathbf{e_p}$ at lower frequencies and slightly negative $\mathbf{e_p}$ at 85.5 GHz in the second EOF. Over India, the monsoon in period 1 vs. its break-up in period 2 reflects this interpretation. The contributions of the third EOFs are not significant with explained variances below 6%.

Finally, the precipitation signal can be obtained from $\mathbf{e_p}$ by:

$$PI = < \delta \mathbf{TB_o}, \mathbf{e_p} > \tag{5}$$

where PI represents an index (in units of K) which is positively correlated to rainrate (rather to ice water path).

2.4 TMI-PR co-location

Calibration requires co-location of TMI and PR observations which are recorded along different scan geometries and resolutions. First, the TMI reference resolution was defined to be either that of the 19.35 GHz or the 85.5 GHz channel to investigate the difference. In both cases, the effective field of view (EVOV) was enlarged by a factor of 2.5 to cover the area of which ~98% of the signal are received (vs. 50% from the 3 dB EFOV). The EFOVs are approximated by ellipses and the antenna gain function by Gaussian functions following the orientation of the real EFOVs along the scan. Only those PR pixels which cover the inner PR swath (beams #15-35) and which were registered at 2 km altitude were included to avoid ground clutter effects which increase with nadir angle and closer to the surface. To minimize sampling problems, only TMI-PR data pairs with valid PR retrievals ($LWC_{PR} \geq 0 g/m^3$) covering more than 80% of the TMI EFOV were used.

Principally, rainfall algorithms over land make use of the information contained in the 85.5 GHz TB, thus their reference resolution would be 5 km x 7 km for the TMI given that the surface can be considered homogeneous over the footprint of the lowest employed frequency. Intercomparison of retrievals on the resolution of the 19.35 vs. 85.5 GHz TMI channels with PR estimates indicate, however, that algorithm perfomance decreases with increasing resolution. This is an effect of the parallax effect introduced below and the fact that the physically loose relationship between surface

rainrate and precipitating ice path that improves with footprint size used for averaging (Burose 2000). Consequently, all further results refer to the resolution at 19.35 GHz, i.e., about 18 km x 30 km.

Data from the first day of period 1, i.e., 16 orbits on 18/08/98 were used for the following evaluation. Thus between 1,000 and 10,000 rain contaminated TMI-PR data pairs were available depending on region.

2.5 Parallax correction

An important issue is the projection of all signatures to the radiometer footpoint. If the major signal contribution originates from larger altitudes, the comparison to radar data at the footpoint location may lead to errors in the calibration dataset because the radiation source is located above a different footpoint for off–nadir viewing sensors. This is more serious at higher frequencies because the weighting function peaks at higher altitudes thus further away from the footpoint. A method similar to that of Bauer et al. (1998) was developed here to correct for this effect over land surfaces and with TMI data. For this purpose, radiative transfer simulations based on mesoscale cloud model simulations were carried out using model experiments from the Cooperative Huntsville Meteorological Experiment (COHMEX, Smith et al. 1992), the Cooperative Convective Precipitation Experiment (CCOPE, Johnson et al. 1993), and the Convection Profonde Tropical Experience (COPT-81, Redelsperger and Lafore 1988). The quasi-three dimensional radiative transfer model of Bauer et al. was employed with the TMI observation specifications, varying surface conditions, and observation geometries (i.e. TMI overpass directions).

The centers of gravity, z_{CG}, of the weighting functions were calculated providing a measure of the altitude of the major signal contribution. From all simulations, a regression-type relation was derived to serve as an estimator of z_{CG} from TMI observations. The PR observations have to be shifted towards the sub-satellite point by:

$$\begin{aligned} d_{CG} &= R_e\,\beta \approx z_{CG} \\ \beta &= \frac{1}{2} sin^{-1}\left[\left(\frac{R_e}{R_e + z_{cg}}\right)^2 - 1\right] \end{aligned} \tag{6}$$

where $R_e = 6370km$ denotes the earth's radius and β is the angle between earth's center, EFOV footpoint and corrected footpoint of the raincloud. In non-raining conditions, d_{CG} has to be 0 while in tropical convection it may reach values of up to 15 km. In any case, the accuracy of this correction depends on the representativity of the cloud simulations keeping in mind that all model clouds represent rather strong convection with significant amounts of cloud ice.

Fig. 5 compares the correlation coefficients between PI and rain liquid water content obtained from PR data (LWC_{PR}) before (left column) and after (right column) correction using regressions for z_{CG} from all three cloud model simulations seperately and together. The x–axis represents the z_{CG}–intervals to which the correction is limited. The general increase of correlation with altitude range indicates the increase of the precipitation signal in the PI with increasing convection intensity. For example, over India for $z_{CG} \in [4 - 6km]$, the parallax correction improves the correlation between PI_{TMI} and LWC_{PR} by 0.05 applying the CCOPE or COPT–81 regression. It is evident that CCOPE and COPT–81 simulations perform better over all regions, except over South America where COHMEX shows higher correlations. COHMEX represents the deepest isolated convection among the simulations with large amounts of graupel. The intercomparison shows larger z_{CG} over South America than over the other regions, i.e., the correlation curves do not show the same saturation as the others. The improvement obtained from the parallax correction becomes evident for altitudes above 4 - 6 km, except over Africa and South America. Based on these results, the parallax correction was applied only for $z_{CG} > 5$ km when calculated from the COPT-81 simulation.

2.6 Heidke skill score

As in Conner and Petty (1998), the Heidke skill score (HSS) was employed to quantify the accuracy of rain detection from both PR and TMI:

$$HSS = \frac{2(AD - BC)}{B^2 + C^2 + 2AD + (B + C)(A + D)} \quad (7)$$

where A/D denote the number of cases where both TMI and PR gave precipitation / no precipitation while B/C are the number of cases where TMI predicted no rain / rain and PR observations showed rain / no rain, respectively. HSS = -1 would describe negative skill, HSS = 0 is no skill, and HSS = 1 is perfect skill. To extend its application beyond rain identification, the datasets were classified into intensity ranges with a lower threshold. Thus, A, B, C, and D depend on algorithm threshold and LWC_{PR}:

$$\begin{aligned} A(i,j) &= \sum_{k=i}^{m}\sum_{l=j}^{n} s(k,l) \quad (8)\\ B(i,j) &= \sum_{k=i}^{m}\sum_{l=1}^{j-1} s(k,l)\\ C(i,j) &= \sum_{k=1}^{i-1}\sum_{l=j}^{n} s(k,l)\\ D(i,j) &= \sum_{k=1}^{i-1}\sum_{l=1}^{j-1} s(k,l) \end{aligned}$$

where s (k,l) denotes the number of counts with indices 'i, k' referring to PR rain LWC (in g/m^3) and 'j, l' referring to algorithm threshold (in K). (m, n) denote maximum numbers of intervals for each quantity. Maximum HSSs per LWC threshold as well as correlation coefficients of the total sample were also calculated. Since the frequency distribution of TB depression due to scattering is more or less flat while that of LWC_{PR} rather follows a logarithmic behaviour, intervals for LWC_{PR} were defined from $log_{10}[LWC_{PR}]$. This also enhances the sensitivity of HSS to lower rainfall intensities.

The interpretation of (7) and (8) in this context is that, for example, A (i,j) gives the sum of samples above a given rain LWC and algorithm threshold, i.e., the weight for a positive skill above (i,j). B represents the sum of samples above a given rain LWC and below the algorithm threshold, i.e., a negative skill with respect to rain above (i) and TBs below (j). C and D work similarly with respect to algorithm thresholds.

2.7 Other algorithms

For comparison, algorithms - originally developed for the Special Sensor Microwave / Imager (SSM/I) – were employed due to their simple coding and general availability (e.g. as part of the standardized products provided by the Global Precipitation Climatology Project, GPCP). The basic difference between the two instruments are their spatial resolution and the replacement of the 22.235 GHz SSM/I channel by the 21.3 GHz TMI channel. Due to the small cloudfree atmospheric signal contribution over land surfaces, the latter effect should be small. Since the resolution of the PR product is rather large (2.5 x EFOV dimensions of TMI 19.35 GHz channel), the difference between sensor imaging is also considered of minor impact.

The NOAA / Satellite Research Laboratory algorithm (NOAA/SRL, Grody 1991, Ferraro and Marks 1995) involves a stepwise screening of different surface types and precipitation depending on

TABLE 1. Correlation coeffcients between LWC_{PR} and TMI precipitation indices (PI = eigenvector index, SI = scattering index, 2C = two-channel index, GS = 85 GHz index, n = sample size).

Region	n	PI	SI	2C	GS
Africa	3576	0.90	0.86	0.85	0.89
S. America	10077	0.60	0.70	0.70	0.65
India	1037	0.70	0.59	0.55	0.63
N. America	6686	0.83	0.78	0.73	0.82

their frequency dependent emission and scattering properties. Both screening and rainrate estimation use a scattering index (SI) defined as the difference between the predicted TB at 85.5 GHz using 19.35 and 22.235 GHz TBs and the observed 85.5 GHz TB. The prediction is for non-raining and non-scattering scenes thus the departure is a measure for rain intensity once scattering surfaces are excluded. The NASA Goddard Scattering algorithm (GSCAT, Adler et al. 1993) originates from combined mesoscale cloud - radiative transfer simulations and calibrates $GS = 262K - TB_{85}$ linearly to surface rainrate. Finally, the Conner and Petty 2C algorithm simply compares TB differences at 37.0 and 85.5 GHz with those from the background field. Again, the TB departure represents the precipitation signal. SI and GS also provide rainrates when used with their calibration coefficients, however, since we aim at rain detection and PI is not yet calibrated, only indices, i.e, PI, SI, 2C, and GS are compared (all in units K).

3 Results

Fig. 6 shows an intercomparison of precipitation indices from the above algorithms and $LWC_{PR} > 0.01 g/m^3$ for all samples from period 1 and all regions. Sample sizes and correlations over all data pairs are given in Tab. 1. From the scatter diagrams, all algorithms seem to perform similarly; however, PI has a somewhat larger dynamic range in terms of K also indicated by the slightly higher correlation coefficients over all regions except South America Over India the improvement is significant with 0.07. The maximum HSS distributions indicate a larger skill of PI over South America at very low LWCs and over India and moderate LWCs. However, for low to moderate LWCs, PI performed worse over South America. For the remaining cases, PI and GS perform similarly while SI and 2C show a weaker performance. This is an important observation because GS consists of a simple TB difference indicating that over land surfaces lower frequencies than 85.5 GHz contribute very little to rainfall detection. Generally, the skill is weak for low and high LWCs giving best performance for $LWC \in [0.03, 0.3 g/m^3] \approx [0.5 - 8 mm/h]$. Above, the connection between ice water path and rainfall at the surface deteriorates with increasing cloud development stage while below the surface contribution is too strong.

HSSs are displayed in more detail in Fig. 7, here only for PI and GS. Both techniques show highest skill scores (> 0.8) over Africa for the above mentioned LWC range. The more shallow convection over India during the monsoon period reduces HSS and correlations while North and South America are represented similarly. PI shows some skill at very low LWCs over South America as well as Africa; however, more data has to be analyzed to investigate this feature. Another observation is the non-linear relation between indices and LWC_{PR}. Since GSCAT (based on GS) employs a linear calibration to rainrate while SI does not, larger differences can be expected once rainrates are compared. Here, HSS offers a tool for determining a calibration for PI which may be updated over time and adjusted to each region with e_p being rather constant for all investigated areas and time periods.

4 Summary and Conclusions

A method for rainfall detection from spaceborne passive microwave observations introduced by Conner and Petty (1998) was adapted with focus on application to TRMM data. The availability of TMI and PR data from the same satellite provides an excellent tool for algorithm testing and calibration. The method is based on the correction of brightness temperature departures from long-term averages for small scale influences by surface skin temperature and moisture thus isolating the precipitation signature. This process is carried out through orthogonalization using eigenvectors obtained from separate datasets which only contain signatures of the effects to correct for. The Conner and Petty technique was modyfied by introducing radiative transfer calculations from cloud-free radiosonde profiles of temperature and moisture and a microwave surface emissivity model. This allows a cleaner isolation of surface effects as opposed to observations. The technique was applied to two periods and four geographical regions to investigate algorithm compatibility.

TMI and PR data were unified to represent average near-surface rainfall intensities (as LWCs) involving a correction for parallax effects. This was developed from combined cloud model– radiative transfer simulations using experiments from various non-hydrostatic models. It was shown that the correction produced improved results once major signal contribution originates from altitudes above 5 km. However, a strong dependence of parallax correction performance on training dataset was found requiring more representative simulations.

Intercomparison of our technique with standard indices (such as NOAA's scattering index or NASA's 85.5 GHz TB index) showed slightly better performance over three out of four regions with best results over India. Heidke skill scores proved to provide a more sensitive intercomparison tool than correlation coefficients only. They also allow the calibration of TB indices to actually provide rainfall rates or LWCs. While the principal component analysis resulted in a rather constant rainfall eigenvector for all regions and both periods, the calibration to rainfall intensity would depend on region and period. Consequently, the following activities have to focus on the non-linear calibration of PI by PR observations covering the investigation of calibration stability and its dependence on region.

Acknowledgements

The authors are grateful for free access to TRMM data through the NASA TRMM program. We are indebted to Jean–Luc Redelsperger (Centre National de Recherche Météorologique, Toulouse) and Greg Tripoli (University of Wisconsin–Madison) for making available the mesoscale cloud model simulations. This research was funded by the Deutsche Forschungsgemeinschaft, contract Ba 1565 1/2.

References

Adler, R.F.; Negri, A.J., Keehn, P.R.; and Hakkarinen, I.M.: Estimation of monthly rainfall over Japan and surrounding waters from a combination of low-orbit microwave and geosynchronous IR data. *J. Appl. Meteor.*, **32**, 335–356, 1993.

Barrett, E.C.; and co-authors: The first WetNet Precipitation Intercomparison Project (PIP–1): Interpretation of results. *Remote Sens. Rev.*, **11**, 303–373, 1995.

Bauer, P.; and Grody, N.C.: The potential of combining SSM/I and SSM/T2 measurements to improve the identification of snowcover and precipitation. *IEEE Trans. Geosci. Remote Sens.*, **33**, 252–261, 1995.

Bauer, P.; Schanz, L.; and Roberti, L.: Correction of three–dimensional effects for passive microwave retrievals of convective clouds. *J. Appl. Meteor.*, **37**, 1619–1632, 1998.

Burose, D.: Schaetzung von Niederschlagsraten ueber Landoberflaechen aus Satellitenmessungen. *Diplomarbeit.* Meteorologisches Institut der Rheinischen Friedrich-Wilhelms-Universit"at Bonn, pp. 79, 2000.

Conner, M.D.; and Petty, G.W.: Validation and intercomparison of SSM/I rain–rate retrieval methods over the continental United States. *J. Appl. Meteor.*, **37**, 679–700, 1998.

Ferraro, R.R.; and Marks, G.F.: The development of SSM/I rain–rate retrieval algorithms using ground–based radar measurements. *J. Atmos. Oceanic Technol.*, **12**, 755–770, 1995.

Grody, N.C.: Classification of snowcover and precipitation using the Special Sensor Microwave Imager. *J. Geophys. Res.*, **96**, 7423–7435, 1991.

Johnson, D.E.; Wang, P.K.; and Straka, J.M.: The numerical simulation of the 2 August 1981 CCOPE supercell storm with and without ice microphysics. *J. Appl. Meteor.*, **32**, 745–759, 1993.

Kummerow, C.D.; Barnes, W.; Kozu, T.; Shiue, J.; and Simpson, J.: The Tropical Rainfall Measuring Mission (TRMM) sensor package. J. *Atmos. Ocean. Tech.*, **15**, 809–817, 1998.

Maetzler, C.; and Standley, A.: Relief effects for passive microwave remote sensing. *Int. J. Remote Sens.*, in press, 2000.

Petty, G.W.: The status of satellite–based rainfall estimation over land. *Remote Sens. Environ.*, **51**, 125–137, 1995.

Redelsperger, J.–L.; and Lafore, J.–P.: Three–dimensional simulation of a tropical squall–line: Convective organization and thermodynamic vertical transports. *J. Atmos. Sci.*, **45**, 1334–1356, 1988.

Smith, E.A.; Cooper, H.J.; Tripoli, G.J.; and Xiang, X.: Foundations for statistical–physical precipitation retrieval from passive microwave satellite measurements. Part I: Brightness–temperature properties of a time–dependent cloud–radiation model. *J. Appl. Meteor.*, **31**, 506–531, 1992.

Smith, E.A.; and co–authors: Results of WetNet PIP–2 project. *J. Atmos. Sci.*, **55**, 1483–1536, 1998.

Figure 1. Average brightness temperatures at 85.5 GHz over selected areas for period 18/08/98-02/09/98.

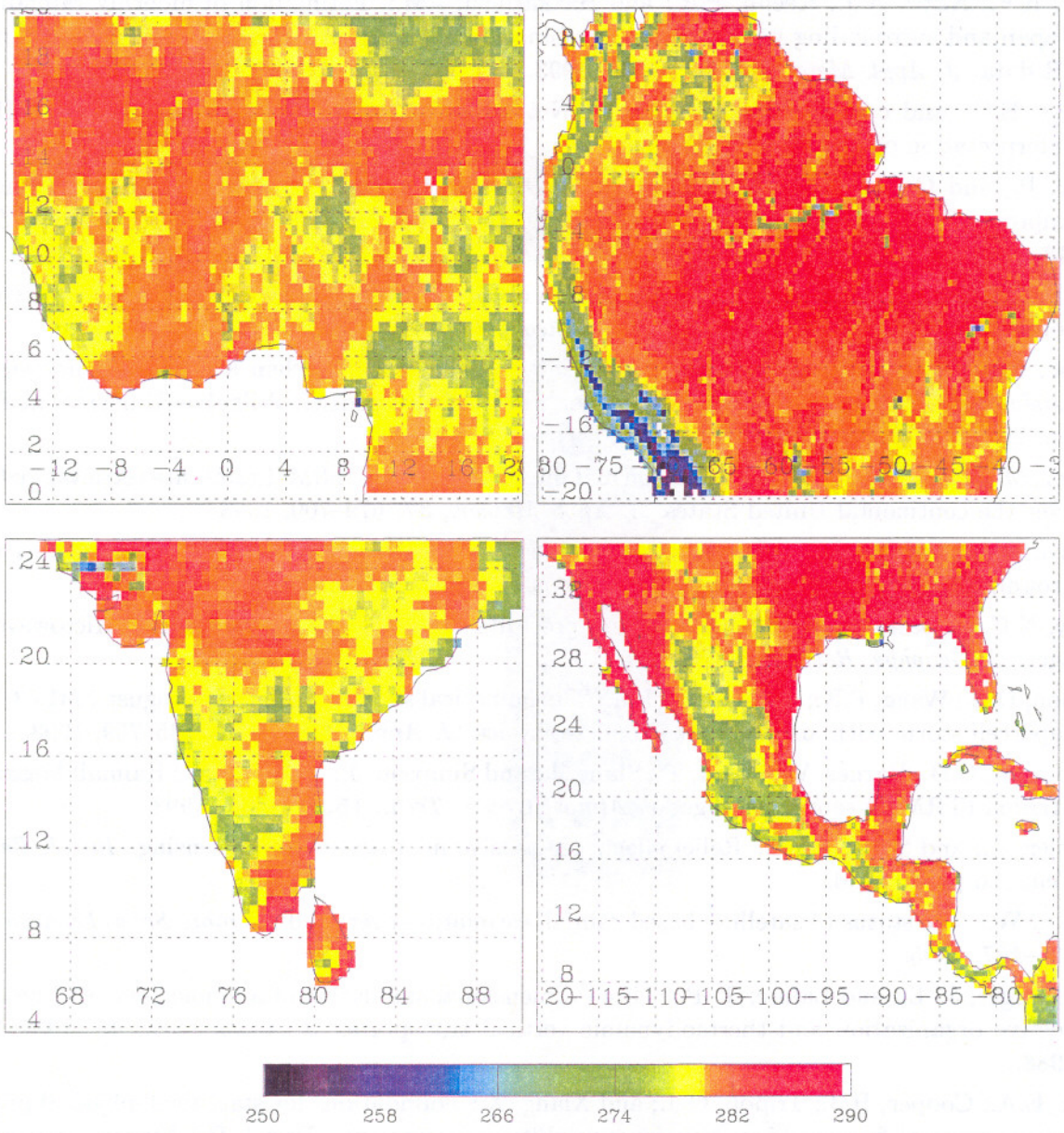

Figure 2. As in Fig. 1 but for standard deviations.

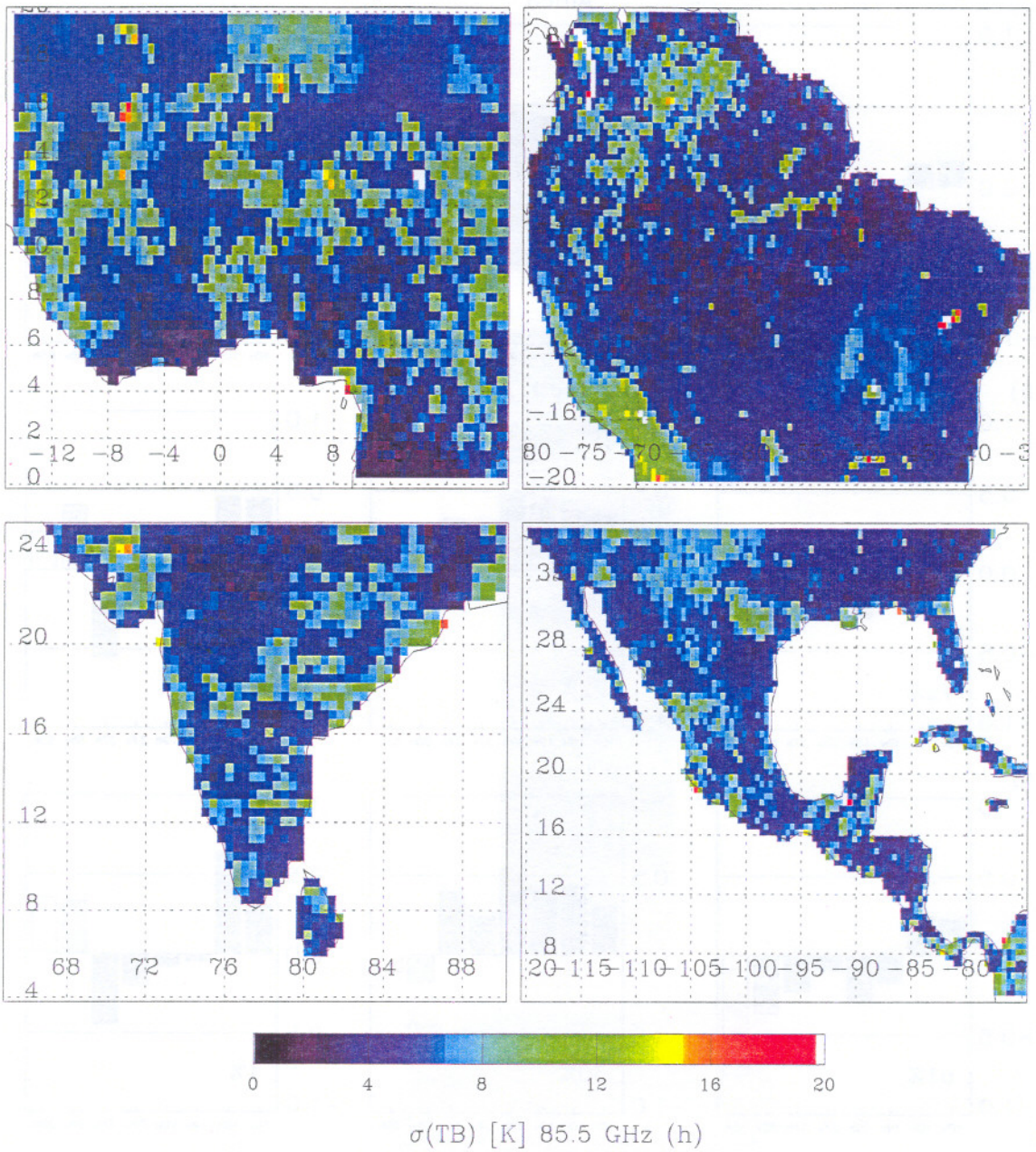

Figure 3. First three EOFs (from left to right) of e_p for selected regions (from top to bottom) for period 18/08/98-02/09/98. Numbers indicate percentage of explained variance.

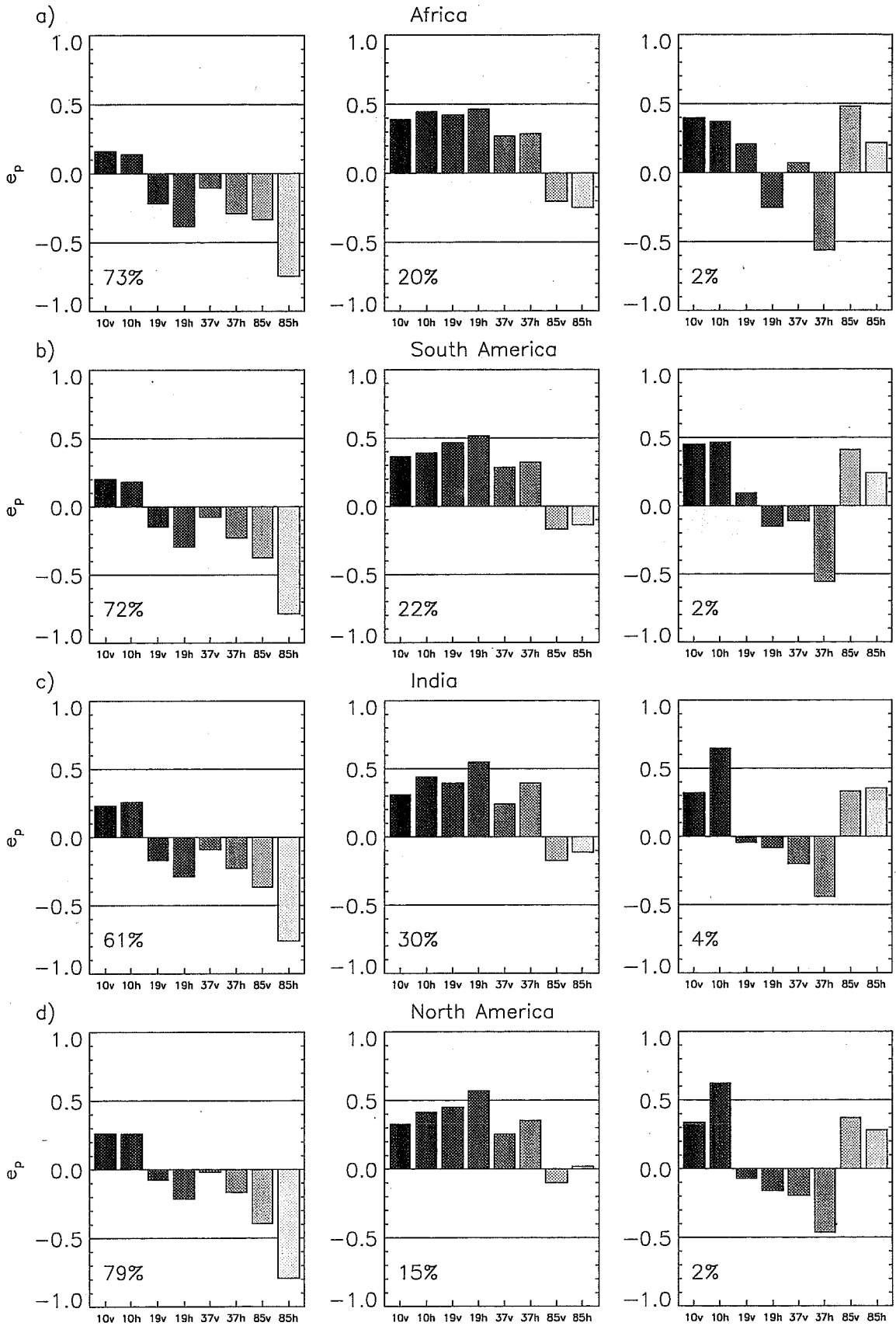

Figure 4. See Fig. 3 for period 13/12/99-05/01/00.

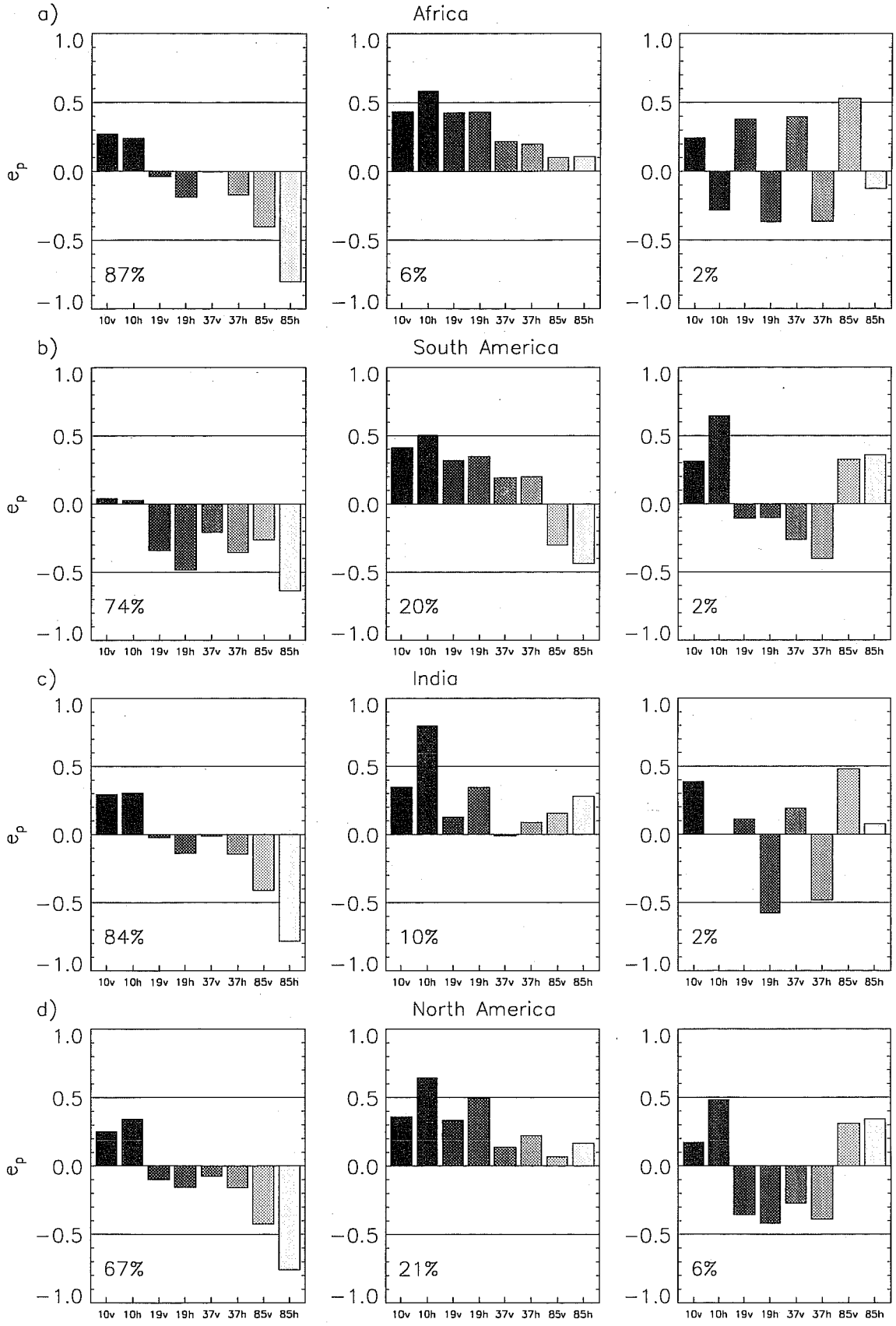

Figure 5. Correlation coefficients between uncorrected (left column) and corrected (right column) PR coordinates per lower altitude threshold applying parallax correction from cloud model simulations.

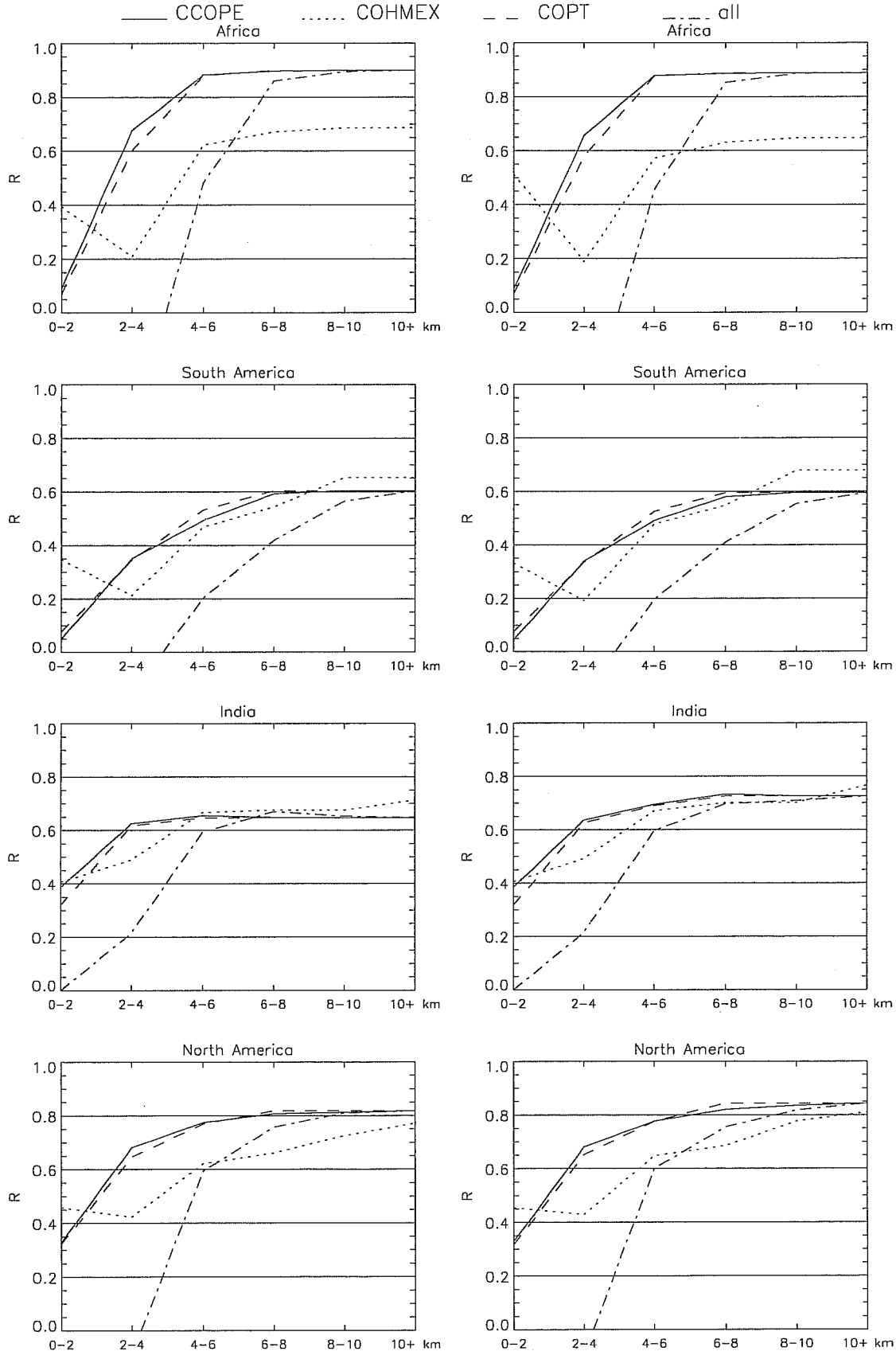

Figure 6. Scatter of precipitation indices vs. LWC_{PR} at 2 km altitude (left column) and maximum Heidke skill scores for all regions from period 18/08/98-02/09/98.

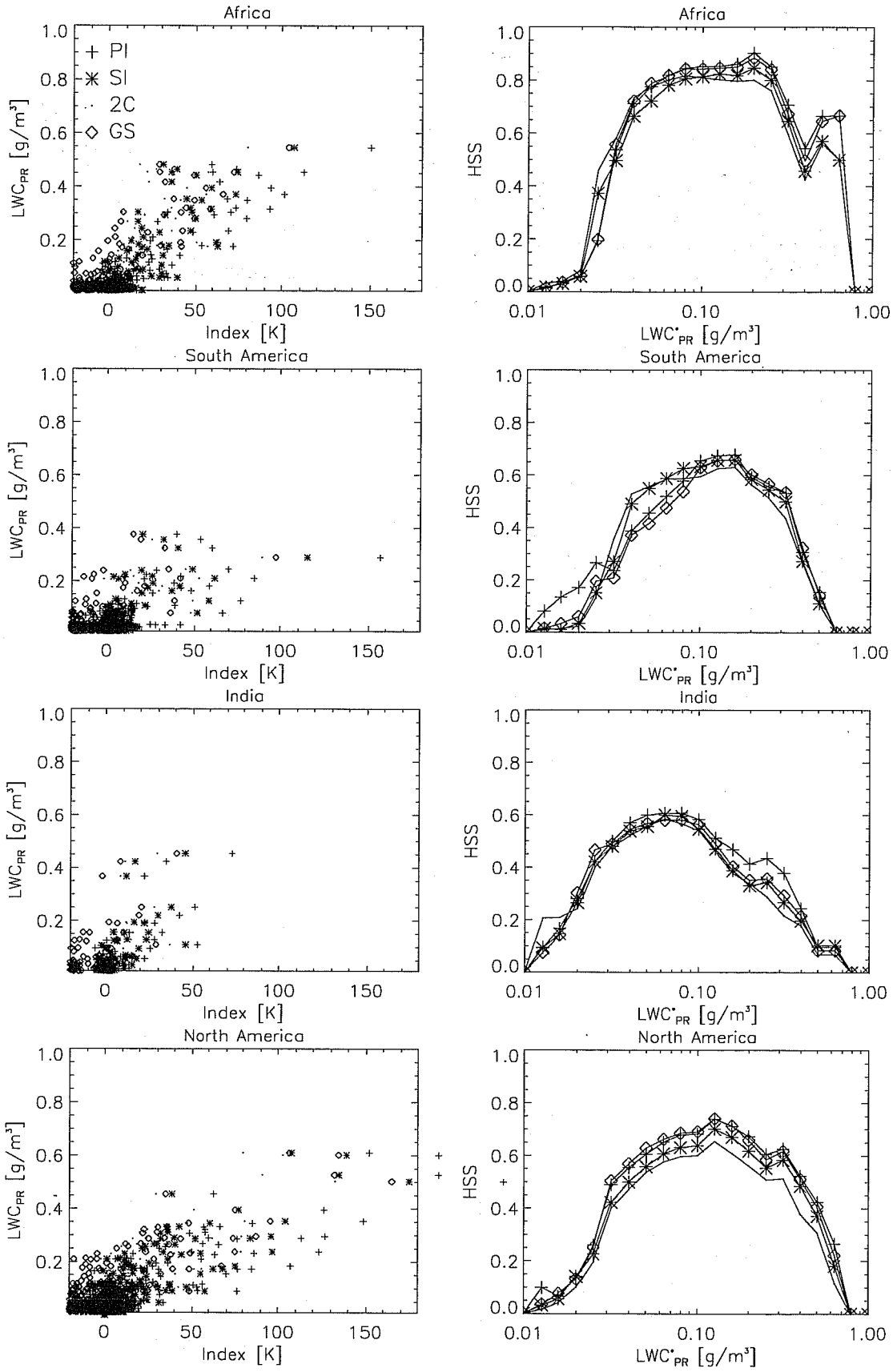

Figure 7. Heidke skill scores for all regions from period 18/08/98-02/09/98 for PI (left column) and GS (right column).